

A Collaborative Computer Aided Diagnosis (C-CAD) System with Eye-Tracking, Sparse Attentional Model, and Deep Learning

Naji Khosravan¹, Haydar Celik², Baris Turkbey², Elizabeth Jones²,
Bradford Wood², Ulas Bagci¹

¹*Center for Research in Computer Vision, University of Central Florida, FL.*

²*Clinical Center, National Institutes of Health, Bethesda, MD.*

Abstract

There are at least two categories of errors in radiology screening that can lead to suboptimal diagnostic decisions and interventions: (i) human fallibility and (ii) complexity of visual search. Computer aided diagnostic (CAD) tools are developed to help radiologists to compensate for some of these errors. However, despite their significant improvements over conventional screening strategies, most CAD systems do not go beyond their use as second opinion tools due to producing a high number of false positives, which human interpreters need to correct. In parallel with efforts in computerized analysis of radiology scans, several researchers have examined behaviors of radiologists while screening medical images to better understand how and why they miss tumors, how they interact with the information in an image, and how they search for unknown pathology in the images. Eye-tracking tools have been instrumental in exploring answers to these fundamental questions. However, most of the studies that utilize eye-tracking technology in radiology screening were not compatible with realistic radiology reading rooms. In this paper, we aim to develop a paradigm shift CAD system, called collaborative CAD (C-CAD), that unifies both of the above mentioned research lines: CAD and eye-tracking. We first design an eye-tracking interface providing radiologists with a real radiology reading room experience. Then, we propose a novel algorithm that unifies eye-tracking data and a CAD system. Specifically, we present a new graph based clustering and sparsification algorithm to transform eye-tracking data (gaze) into a signal model to interpret gaze patterns quantitatively and qualitatively. The proposed C-CAD collaborates with ra-

diologists via eye-tracking technology and helps them to improve diagnostic decisions. The C-CAD learns radiologists' search efficiency by processing their gaze patterns. To do this, the C-CAD uses a deep learning algorithm in a newly designed multi-task learning platform to segment and diagnose cancers simultaneously. The proposed C-CAD system has been tested in a lung cancer screening process (using low dose chest CTs) with multiple radiologists. Promising results support the efficiency, accuracy and applicability of the proposed C-CAD system in a real radiology room setting. We have also shown that our framework is generalizable to other, even more complex, applications with a different screening example: prostate cancer screening with multi-parametric magnetic resonance imaging (MRI). Feasibility of the C-CAD in addressing the unique challenges of MRI and the use of multiple modalities and screens for eye-tracking is presented.

Keywords: Multi-task deep learning, graph sparsification, eye-tracking, lung cancer screening, prostate cancer screening, diagnosis.

1. Introduction

Radiology imaging plays an important role in screening, diagnosis, prognosis, and therapy planning for various cancers. Lung cancer screening with low dose computed tomography (CT) was shown to reduce lung cancer mortality by 20%(Siegel et al. (2017)). Breast mammography for breast cancer screening and multi-parametric magnetic resonance imaging (MRI) for prostate cancer screening are some other notable examples where radiologists search the radiology scans to detect potential abnormalities. Despite promising advances in screening, there remains unsolved problems along with significant sources of errors. An abnormality might be totally missed or misdiagnosed during the screening process. These kinds of errors are called perceptual errors in general. Perceptual errors can be grouped into two main classes: recognition and decision making errors (Kundel et al. (1978)). Overdiagnosis is another significant error leading to unnecessary treatment which can cause even more harm. Prominent evidence for misdiagnosis is that 35% of lung nodules are completely missed during the screening process (Caroline (2014)). Another example in lung cancer screening is the detection of indolent tumors, which do not cause clinical symptoms (Detterbeck et al. (2013)).

To alleviate some of these errors, Computer Aided Detection/Diagnosis

(CAD) systems have been designed for various clinical applications (Firmino et al. (2014); Lemaître et al. (2015); Jalalian et al. (2013)). The CADs are often known as second opinion tools and they generally help in reducing false negative findings such as missing tumors. However, they also have serious limitations such as a large number of false positive findings and high execution times. It is expected that radiologists complement those false positives at least to make the CAD system(s) usable in routine clinical diagnosis, but the use of CAD systems in routine clinical practice has not been found to be feasible by many radiologists, and their use remains as a research tool.

While advances in CAD development continue, vision scientists have focused on exploring human errors in screening (i.e., perceptual errors) for more than three decades (Kundel et al. (1978); Lee et al. (2013); McCreadie and Oliver (2009)). One natural way to explore these perceptual errors is to use eye-tracking technology, which provides insight into image interpretation by modeling perceptual and cognitive processes of radiologists. The vision literature that uses eye-tracking in radiology scans is vast (Al-Moteri et al. (2017); Kok and Jarodzka (2017); Venjakob (2015); Drew et al. (2013a); Manning et al. (2006); Littlefair et al. (2017); Tourassi et al. (2013)). However, most of the literature in this area fails to provide: (1) a real radiology room experience for radiologists, (2) quantitative modeling and comparison of eye-tracking data, and (3) exploration of eye-tracking tools' potential to compensate for CAD errors. In this paper, we introduce a paradigm-shift effort for creating a new CAD system that utilizes eye-tracking technology as a collaborative tool between radiologists and CAD systems. The rationale behind this idea comes from the fact that radiologists are good at eliminating false positives, which CADs often fail to achieve this at a human level performance. On the other hand, CADs capture missing tumors better than the human observer. Because of this natural interaction between radiologists and CAD, we call the proposed technology collaborative CAD (C-CAD).

Mainly, we target reducing the significant drawback of CAD systems (i.e., false positive findings) by developing an accurate and efficient deep learning algorithm that accepts input from an eye-tracking device, and the produced results are presented to radiologists for their diagnostic evaluations. We hypothesize that combining the strength of radiologists and CAD systems will improve the screening/diagnosis performance of overall CAD systems. To test this hypothesis, we have conducted a lung cancer diagnosis screening experiment (with low dose CT scans) based on eye-tracking data recorded from multiple radiologists. We have also showed the applicability of our framework

to other imaging modalities and settings (i.e., multi-modality MRI), where multiple screens were used to conduct prostate cancer screening. We chose lung and prostate cancer due to their high rate of mortality and growth in 2017, thus confirming their clinical importance (Siegel et al. (2017)).

1.1. Related Works.

We are not aware of any study that combines all the topics of eye-tracking, graph sparsification and multi-task image analysis in a single framework to make a CAD system; therefore, noteworthy studies as compared to individual steps of our algorithms are summarized. Since we focus on two clinical screening examinations in this study (lung and prostate cancers), studies related to clinical applications will be confined to only these two topics. However, we argue that the method presented here can be generalized to other radiology screening examinations.

Benefits of Screening: According to the American Cancer Society, lung and prostate cancers are the leading causes of death and also the fastest growing cancers in 2017 (Siegel et al. (2017)). Medical imaging helps early detection of cancers, but in a recent lung cancer screening clinical trial, it was found that approximately 35% of lung nodules are missed during the screening process by radiologists (Caroline (2014)). Previous studies have shown that early diagnosis of cancers may have a greater impact on the population (Siegel et al. (2017); Caroline (2014); Samuel G. Armato et al. (2002)). However, too many open questions remain in screening examinations. For instance, definition of the at-risk population affects the patient’s inclusion in the study. Timing and intervals of screening are adjusted by clinical trials, but there is no optimal method yet to justify these selections. Nevertheless, even in these suboptimal conditions, exciting research is ongoing in this field, thanks to more advanced CT scanners and development of computerized image analysis methods. Computer aided detection (CAD) systems have been shown to be useful in reducing false negative (missed tumor) cases, but the main issue with all these CAD systems is the presence of a high false positive rate (Al Mohammad et al. (2017)). For instance, when an automated lung nodule detection method was used in a study by Samuel G. Armato et al. (2002), 84% of the missed lung cancers were marked by the computer. Despite this catch, the false-positive rate was very high: 28 false positive findings per scan.

CAD systems in the deep learning era: Conventionally, CAD systems are designed to assist radiologists in making accurate and fast diagnos-

tic decisions by minimizing the number of false negatives, and increasing the true detection rate of tumors. In recent years, deep learning based algorithms revolutionized many fields including medical image analysis applications. In conventional CAD systems (i.e., prior to the deep learning era), hand-crafted feature design/extraction followed by a feature selection and classification scheme were the main steps. However, with the success of deep learning, this strategy has moved from *feature engineering* to *feature learning*. In very recent frameworks, Convolutional Neural Networks (CNN) have been used for feature extraction and off-the-shelf classification methods in most CAD systems (van Ginneken et al. (2015); Ciompi et al. (2015); Tsehay et al. (2017a); Le et al. (2017)). In this line of research, for instance, Hua et al. proposed using a Deep Belief Network and a CNN for lung nodule classification (Hua et al. (2015)) while Kumar et al. used deep features extracted from an autoencoder to classify nodules into malignant and benign (Kumar et al. (2015)). Deep learning for lung cancer detection has also been used as part of a screening strategy (Roth et al. (2016); Setio et al. (2016)).

In our previous works, we have developed various deep learning networks for lung cancer diagnosis (Buty et al. (2016); Hussein et al. (2017b,a)). In those works, we have first incorporated shape information of the lung nodules to improve diagnostic accuracy (Buty et al. (2016)). In another approach, we investigated Gaussian Process algorithms along with CNN to incorporate radiographical interpretations of nodule appearances to improve diagnostic decisions as well (Hussein et al. (2017b)). Later, we improved our network (called *TumorNET*) by converting the CNN into a multi-task deep learning strategy (Hussein et al. (2017a)). The literature pertaining to lung nodule detection and characterization via CNN is vast. A brief overview of some architectures used in this field can be found in (Shin et al. (2016)). Specific to prostate cancer detection from radiology scans, recent works, published by our collaborators at NIH, investigated the application of CNNs using Multiparametric MRI (Tsehay et al. (2017b)) as well as a semi-supervised approach for biopsy-guided cancer detection using a deep CNN (Tsehay et al. (2017a)). Deep learning has also been used as a feature learning tool for various applications such as MR prostate segmentation (Guo et al. (2016)).

It is beyond the scope of this study to enlist all of the relevant papers in deep learning based CAD systems in lung and prostate cancers in this manuscript. Herein, we devise a totally new approach for a CAD design, where deep learning is the part of a collaborative learning strategy.

Visual Search Studies in Radiology: A key aspect of biological vi-

sion studies was to understand perceptual errors and how radiologists search the scan for finding abnormalities. Those studies have extensively benefited from different eye-tracking technologies (Venjakob and Mello-Thoms (2016)). Comparison of the visual search patterns of radiologists, and inferring local and global information from those patterns have accelerated the research in this field and led to better understanding of the differences between expert and novice readers/radiologists, and general strategies for visual search in radiology scans. Some of these studies date back to the 1960s. In spite of decades of work in this field, available methods in the literature fail to provide: (1) a real radiology room experience for radiologists, and (2) a quantitative modeling and comparison of eye-tracking data, and (3) exploration of eye-tracking tools' potential to compensate for CAD errors. In particular, the interaction between radiologists and computers (either simple PACS or CAD systems) remain untouched except by a few seminal image analysis studies (Drew et al. (2013b); Khosravan et al. (2016); Venjakob et al. (2016)).

Challenges: Realistic radiology experience with eye-tracking data was not achieved, mainly because of technical complexities. Eye-tracking systems record data in 2D and having a 3D system needs a very exact synchronization. Furthermore, one of the main challenges of quantitative modeling and comparison of gaze data stems from the difficulty of representing, analyzing, and interpreting dense eye-tracking data. It is not only technically challenging, but also computationally demanding (Venjakob and Mello-Thoms (2016)). The closest study addressing these problems was conducted by (Drew et al. (2013b)) who proposed the famous *scanning and drilling* paper analyzing gaze patterns at the global level. While *scanners* examine one slice of a radiology image more explicitly before moving to the next one, *drillers* keep going forward and backward in slices, moving through a 3D stack of the image. However, quantitative analysis of search patterns at the global and local level has never been addressed. We believe that such mapping will be extremely useful since it can serve as a natural interface between radiologists and CAD system, and that details of the gaze patterns will be used to guide a CAD system when it is necessary. In other words, it is not possible to benefit from human visual search in CAD systems if search patterns are represented only at the global level. This forms the major challenge of the problem depicted in (3).

What we propose? In this study, we address these challenges by (1) developing an eye-tracking interface that provides a real radiology reading room experience and (2) performing an attention based clustering and spar-

sification of dense eye-tracking data. Our proposed algorithm preserves topological properties of the data while reducing its size significantly. This allows us to quantitatively compare global search patterns of radiologists, extract radiologist’s regions of interest (ROI) based on their level of attention during the screening process (local), and to combine this information with image content to do different image analysis tasks inside ROIs. Radiologist’s gaze data is represented as a graph and sparsified using the proposed attention based algorithm. Finally, a 3D Deep Multi-Task CNN is presented to perform false positive removal (FP removal) and segmentation jointly inside the extracted ROIs. An overview of the proposed framework (C-CAD) is illustrated with lung cancer diagnosis as an example (see Fig. 1). Details of each module in the proposed framework are explained in the following sections.

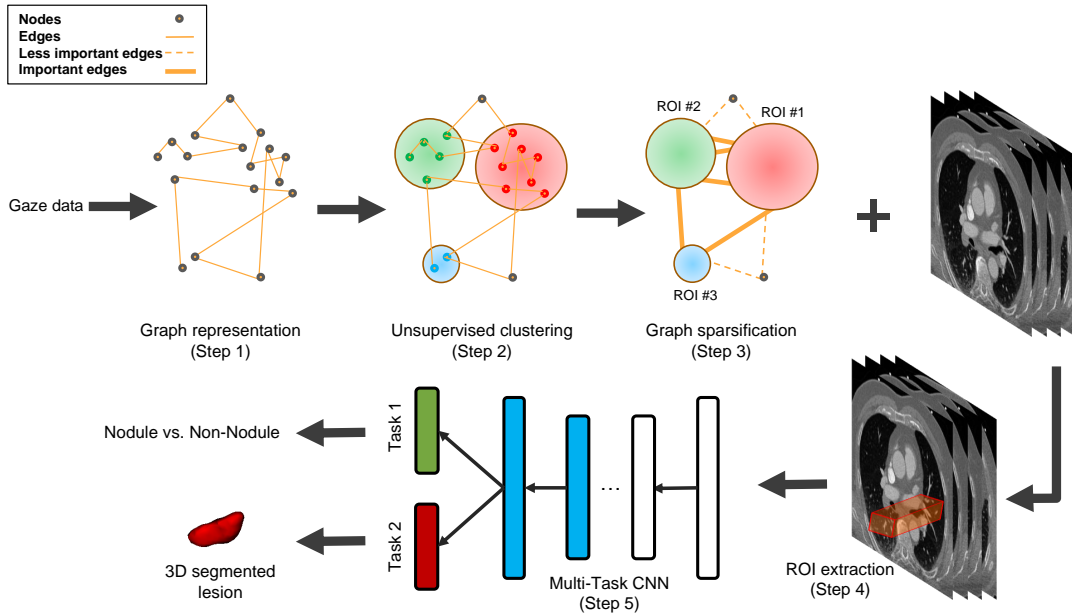


Figure 1: To extract radiologist ROIs the dense eye-tracking data goes through a clustering and sparsification algorithm. After extracting ROIs a 3D multi-task CNN is used to perform FP removal and segmentation of lesions inside the ROIs, jointly.

Our work is built upon our previous effort published in (Khosravan et al. (2016)). In our previous work, we first thresholded the eye-tracking data by its time component to define potential attentional regions. Then, these regions (ROIs) were processed with computer vision based saliency models to remove some of the false positive regions from considerations. Final ROIs

were used for image analysis, particularly for segmenting lung pathologies using attention. A 2D random walk algorithm (Grady (2006)) was utilized to segment those ROIs by combining visual saliency and visual attention information as seeds of random walk algorithm. The average dice similarity of 86% was achieved. In the current study, we significantly improved our design into a new level with multiple novel contributions as defined below.

1.2. Our Contributions:

We believe that our work has significant broader impacts in radiology and imaging sciences and introduces several technical innovations as summarized below:

- A key aspect of any interactive system is to provide a natural feeling to the user. Having this natural feeling plays a crucial role specifically in the field of radiology, as imposing any constraint might affect the diagnosis accuracy. The majority of eye-tracking studies are conducted in the laboratory settings and no realistic eye-tracking based 3D screening experiment is reported in the literature. Our work fills this research gap and provides a natural (realistic) interaction framework.
- We propose a new attention based data sparsification method applied to gaze patterns of radiologists which allows local and global analysis of visual search patterns based on visual attention concepts. More importantly, sparse representation of gaze patterns help interaction with the newly designed CAD system. The proposed system truly collaborates with its human counterpart (i.e., radiologists); therefore, it is unique and substantially different than currently available second opinion tools. As a proof of concept, we experiment with a lung cancer diagnosis problem using low dose CT scans.
- We develop a new CAD system by proposing the state of the art 3D deep learning algorithm in a newly designed multi-task learning platform where both segmentation and diagnosis tasks are jointly modeled. The proposed system has been tested by radiologists with different years of experience, and robustness of the proposed C-CAD has been demonstrated.
- We extend the proposed eye-tracking based CAD system into a multi-modality image analysis framework where users can utilize multiple

screens as in prostate screening with multi-parametric MRI. To the best of our knowledge, this is the first study in the literature considering multi-modality MRI and multiple screens in the eye-tracking platform too.

In Section 2, we describe the proposed hardware and software integration, details of data acquisition parameters, the proposed data representation technique with sparsification, and multi-task learning based deep learning algorithm for tumor diagnosis. In Section 3, we report validation of the sparsification experiments followed by a lung cancer diagnosis experiment conducted with the whole system (C-CAD). In Section 4, we introduce the potential of the proposed C-CAD system to handle multi-modality images and multi-screen based eye-tracking and image analysis in general. We conclude the paper with a discussion and summary.

2. Methods

2.1. Data acquisition and Eye-Tracker:

In this study, a FovioTM Eye Tracker remote eye-tracker system (Seeing Machines Inc, Canberra, Australia) was used. We collected eye tracking data using EyeWorksTM Suite (*v.3.12*) on a DELL Precision *T3600* using a Windows 7 operating system on an Intel Xeon CPU *E5 – 1603 0 @ 2.80GHz* with *8GB* of RAM. Figure 2 illustrates integration of Eye-Tracker into our system. Using EyeWorksTM, eye movements were recorded by two synchronized, remote eye-trackers at *60Hz*. All stimuli were presented at a resolution of 1280×1024 on a DELL 19" LCD monitor. We utilized a *60Hz* FOVIO eye-tracker manufactured by Seeing Machines and verified calibration through a five-point calibration procedure in EyeWorksTM Record prior to the task. Calibration was considered sufficient if the dot following the eye movement trajectory was sustained (indicating that the eye movement monitor was not losing tracking) and if the calibration dot was accurate (falling on the calibration check targets at the center and corners of the screen when the participant was instructed to look at them, with inaccuracy of up to one centimeter for the upper two corner targets). The eye-tracker was located between *9.5 cm* and *8 cm* beneath the bottom of the viewing screen (eye-tracker was placed just under the viewing area and at a 25 degree angle with respect to the monitor.). Following calibration, participants completed the

task as described above. After completing this task, the FOVIO was recalibrated before moving on to a Smooth Pursuit task. Upon completion of screening, the experimental portion of the study was complete and subjects discussed the study with the experimenters before leaving. From consent to debriefing, the study duration spanned roughly 45 *minutes*. Custom made DICOM viewing software was built on Medical Image Processing, Analysis and Visualization software (MIPAV CIT, NIH, Bethesda, MD).

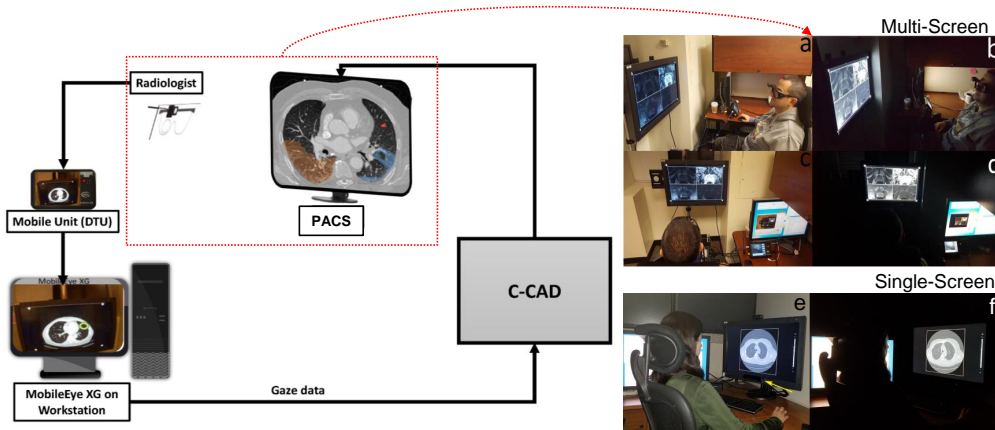


Figure 2: A representation of the Eye-Tracking system in a realistic radiology setting is illustrated. Eye-Tracking glasses, the connection to the mobile workstation, and the C-CAD system are integrated into the PACS system directly as shown on the left. Screening experiments in normal light and dark radiology rooms for single and multi-screen experiments are shown on the right.

In our proposed framework, eye-tracking data goes through five steps to be converted from a dense graph into a set of decisions and segmentation masks on the lesions inside ROIs: *Step 1)* The data is represented with a graph. *Step 2)* An unsupervised clustering method is applied to the graph nodes. *Step 3)* Our proposed novel attention-based sparsification algorithm is applied to the graph to reduce redundant information. *Step 4)* Radiologist’s Regions of Interest are extracted based on the level of attention, and *Step 5)* Our Deep 3D multi-task Convolutional Neural Network (CNN) is used to jointly decide about lesions as a nodule or non-nodules (FP removal) and segment potential abnormalities inside suspicious areas. (See Fig. 1 for the overview of the proposed system for an example application).

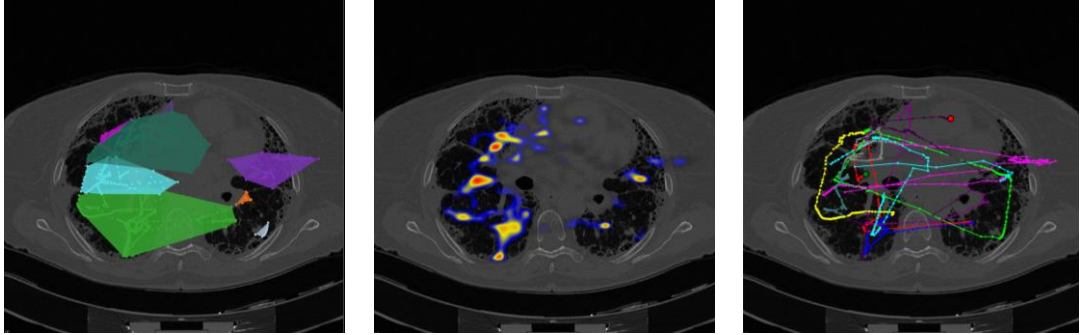


Figure 3: Eye-tracking data recorded from lung cancer screening. Low-dose CT is used in a single screen. Gaze patterns (right), heat maps of gaze patterns (middle), and coverage area of the gaze patterns (left) are illustrated.

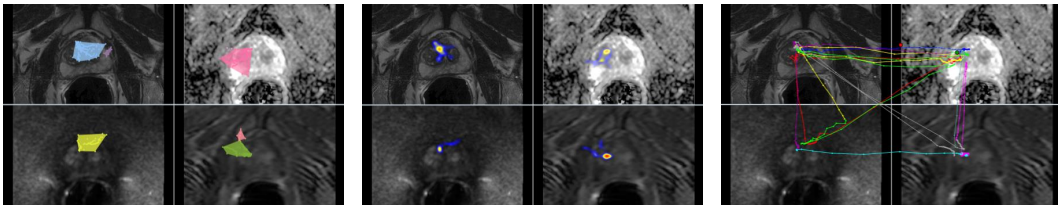


Figure 4: Eye-tracking data recorded from prostate cancer screening. Multi-parametric MRI is used in four screens (left upper: T2-weighted (T2w), right upper: apparent diffusion coefficient (ADC) map, left lower: diffusion weighted imaging (DWI), right lower: dynamic contrast enhanced (DCE) maps). Gaze patterns across different screens and the paths are illustrated for an example screening task. Gaze patterns (right), heat maps of gaze patterns (middle), and coverage area of the gaze patterns (left) are illustrated.

2.2. Step 1: A graph representation of the eye-tracking data

An example of eye-tracking data recorded from two cancer screening tasks is shown in Fig. 3 and Fig.4 . In each image, 2D images are overlaid with the coverage area (left), heatmap (middle), and scanpaths (right) representations inferred from the gaze patterns. Once gaze patterns are recorded, they are dense, hence, difficult to analyze (See Fig. 5). The aim in data sparsification is to represent the data in a way that can be processed easily and efficiently. To this end, we propose to use graphs to represent eye-tracking data and reduce its size without distorting the topology of the data structure.

Graph theory is concerned with a network of points (nodes or vertices) connected by lines (edges). It is a well-established branch of mathematics and it has numerous successful applications in diverse fields. Formally, a

graph (G) refers to a set of vertices (V) and edges (E) that connect the vertices, and it is represented as $G = (V, E)$. In the current problem, a graph representation is a perfect choice for eye-tracking data because gaze locations (i.e., fixations) can easily be stored as vertices while path/directions (i.e., saccades) between gaze locations can be stored as edges in the graph. An example of a 3D graph representation of gaze patterns obtained from a lung cancer screening experiment using volumetric low-dose CT scans is illustrated in Fig. 5(a). A zoomed version of the graph indicates dense data points and edges between them. For simplicity, edges are shown as undirected.

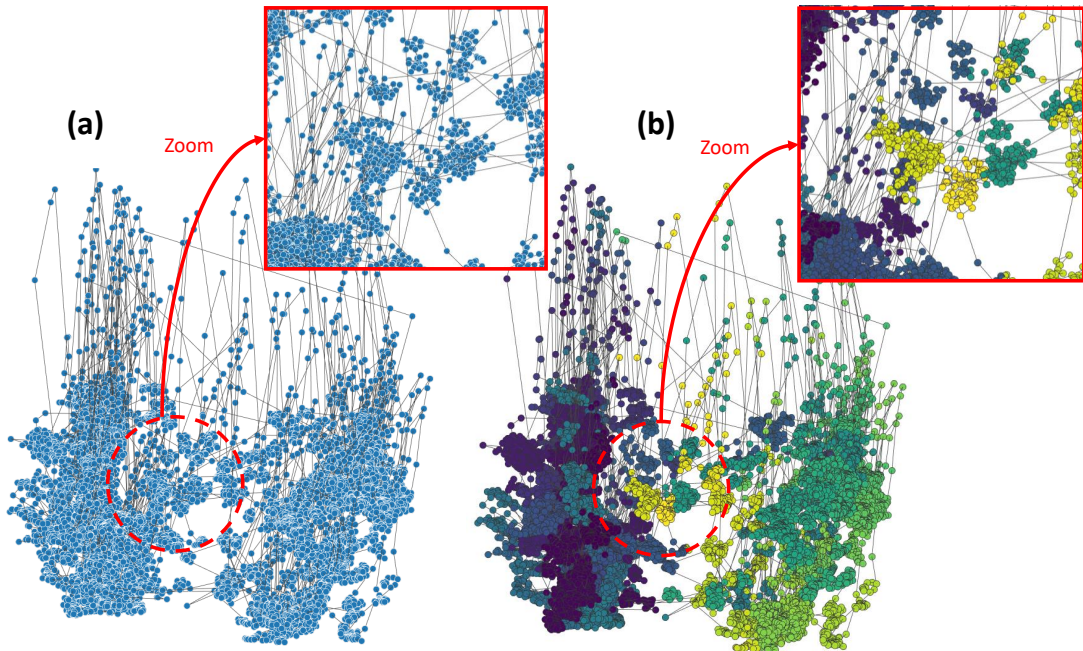


Figure 5: (a) Graph representation of visual search patterns from a lung cancer screening experiment. (b) Clustering helps to group gaze points to define attention regions. Colors indicate different clusters.

Although graph representation allows parameterization of the patterns in the data, its analysis and interpretation are infeasible because the graph includes large amount of nodes and edges as exemplified in Fig. 5. Such graphs are called "dense", and *sparsification* operation can be considered to simplify the data to overcome challenges of the analysis of a dense graph. A graph sparsification algorithm reduces the graph density by omitting unnecessary edges. However, there are challenges and concerns unique to our

problem which makes the conventional sparsification algorithms suboptimal in our case:

- *First*, the constructed graph is consecutive, meaning each edge in our graph connects only two distinct vertices (due to the nature of eye-tracking data). This causes a maximum vertex degree of 2 in our graph resulting in the failure of all current sparsification algorithms to remove even a single edge from our graph. This is because all the edges in our graph are considered equally important for keeping the structure of the graph unchanged.
- *Second*, we are dealing with eye-tracking data which is recorded from radiologists during screening examinations. This adds an extra constraint, which is the radiologist’s attention, that should be taken into account while sparsifying the data. In other words, not only it is important to minimize the graph while maintaining the graph structure, but also to take into account the attention regions of the radiologist. This will make sure that the global visual search pattern and attention regions are both preserved after sparsification.

To overcome these challenges we propose the next two steps of our algorithm to handle the consecutive nature of the data and encountering attention information, respectively.

2.3. Step 2: Unsupervised clustering of the graph nodes

In the gaze data, which is represented as a graph, direction between nodes does not allow the existing sparsification methods in the literature (Batson et al. (2013)) to reduce any edges from the graph as all edges are considered equally important in the current problem, preserving the graph’s topology. To overcome this problem we propose to apply a clustering algorithm to graph vertexes and reconstruct the graph. Since the number of clusters in our problem is unknown, we propose to use an unsupervised clustering method. Also, since gaze patterns are dense, it is desirable that the clustering algorithm is time-efficient.

There exists a great number of clustering methods in the literature due to its applicability in many fields. Each algorithm has advantages and disadvantages. For instance, k-means algorithm may require to pre-specify the number of clusters. On the other hand, unsupervised clustering algorithms omit the choice of cluster numbers, but they have difficulty in determining

similarity of clusters. In other words, unsupervised clustering algorithms often have subjective measures for partitioning the data into distinct groups. Hence, many efforts are spent on designing such measures. The choice of this similarity measure (or called dissimilarity metric in the same fashion) is very important, as it has a strong effect on the resulting groupings. In the current problem, we make a domain-specific definition of *similarity* for gaze patterns. Simply, we propose to use distance between gaze points as a similarity measure. This is because if radiologists spend more time in screening for a particular region (i.e., attention region), then the data collected from those regions are dense and in close vicinity of each other. Likewise, if the distances between gaze locations are far, it can be safely assumed that a different attention region is being examined. Given the fact that, there will be some heterogeneity in distance measurements, it is still a reasonable assumption to use it, as is common in most unsupervised clustering algorithms. However, any clustering algorithm with a distance based similarity metric will not be an optimal choice in our case since the data is extremely dense, and we desire the algorithm to run in linear time while processing large amounts of data.

We hypothesize that the Balanced Iterative Reducing and Clustering using Hierarchies (BIRCH) algorithm can be a good fit for our purpose because it is time-efficient (linear time), unsupervised, and local (Zhang et al. (1996)). BIRCH uses a Cluster Feature (CF) = (N, LS, SS) to make a large clustering problem tractable by concentrating on densely occupied portions. For N data points in a given cluster X_i , $LS = \sum_{i=1}^N X_i$, and $SS = \sum_{i=1}^N X_i^2$ are used to measure pairwise distances between data points. N , LS and SS are basically representing norms of the cluster.

This step represents the dense data with a set of attention regions by clustering them into different groups allowing us to modify our graph as follows:

1. all the vertexes pertaining to each cluster are removed except the centroid of the cluster,
2. all the edges that were connecting vertices from different clusters now connect the corresponding centroids, and
3. all the edges that were connecting vertices inside each cluster are modeled as self loops on the centroid (see Fig. 1).

This modification allows the maximum vertex degree of larger than 2 in the graph. The results of clustering on the graph vertexes and the modified graph respectively are shown in Fig. 5. (Note: the self loops on cluster centroids are not shown in the modified graph for the sake of visibility). Spectral sparsification algorithms now can be used to further reduce the data.

2.4. Step 3: Attention based graph sparsification

In the previous step, we simplified our graph by eliminating vertices inside each cluster and represent them by a centroid. This step will switch the attention mechanism from vertices to clusters, meaning that the attention region is now represented by clusters. Graph sparsification methods, on the other hand, eliminate edges and convert a dense graph G into a sparse graph S .

In our proposed method, we intend to preserve the structural similarity between the sparsified and original graphs; therefore, spectral sparsification algorithms are more suitable than the other kinds. It is mainly because many graphs can be characterized better with spectral estimations where spectral information is obtained by a normalized adjacency matrix, which is normalized by its edges and subtracted from the identity matrix. In our problem, another constraint is to have a linear or nearly-linear sparsification algorithm to make the whole dense data analysis efficient. Due to these two constraints (being fast and intention to preserve structural similarities), we adapted Spielman’s nearly-linear time spectral graph sparsification method with a novel weight parameter, w , to reflect attention regions inferred from eye-tracking data (Spielman and Srivastava (2011)). This particular spectral sparsification algorithm forces the Laplacian quadratic form of the sparsified graph to be a σ – *spectral approximation* of the original graph (Spielman and Srivastava (2011)) and preserves the structural similarity between the sparsified and original graph. Note that the spectral sparsifier is defined as a subgraph of the original whose Laplacian quadratic form is approximately the same as that of the original graph on all real vector inputs, as proved by (Spielman and Srivastava (2011)). That is, if the Laplacian (i.e., spectral properties) matrix is preserved, the structural similarity is preserved.

The Laplacian matrix of a weighted graph $G(V, E, w)$ is defined simply as:

$$L_G(i, j) = \begin{cases} -w_{i,j} & i \neq j \\ \sum_z w_{i,z} & i = j, \end{cases} \quad (1)$$

where $w_{i,j}$ represents the weight of edge between vertexes i and j . The Laplacian quadratic form of graph G for $x \in \mathbb{R}^V$ can be written as:

$$x^T L_G x = \sum_{i,j \in E} w_{i,j} (x(i) - x(j))^2. \quad (2)$$

Also, let \hat{G} be a σ - *spectral approximation* of G if for all $x \in \mathbb{R}^V$:

$$\frac{1}{\sigma} x^T L_{\hat{G}} x \leq x^T L_G x \leq \sigma x^T L_{\hat{G}} x. \quad (3)$$

In the original implementation of the spectral sparsification algorithm (Spielman and Srivastava (2011)), a weighted graph $G(V, E, w)$ is converted to a sparse graph $S(V, \hat{E}, \hat{w})$ with $|\hat{E}| = O(n \log n / \alpha^2)$ in $\tilde{O}(m)$ time, for a graph with n vertices and m edges, such that

$$(1 - \alpha) \sum_{i,j \in E} w_{i,j} (\delta x)^2 \leq \sum_{i,j \in \hat{E}} \hat{w}_{i,j} (\delta x)^2 \leq (1 + \alpha) \sum_{i,j \in E} w_{i,j} (\delta x)^2, \quad (4)$$

where α is the sparsification parameter and δx denotes $x(i) - x(j)$. This method samples edges from G with a probability proportional to $w_{i,j} \cdot r_{i,j}$, where $r_{i,j}$ represents effective resistance corresponding to the edge. Note that *effective resistance* is nothing but a distance measure, inspired by the homology (i.e., correspondence) between a graph and an electrical network.

We modified the spectral sparsification approach according to our unique problem by adding a novel weight function to it. We presented the radiologists' level of attention on different regions by the edge weight between those regions. These weights are further used as a probability measure to define their importance. More important edges are the edges connecting regions with more attention indicating dense visual search patterns. We transferred these rationale into our graph using two primary parameters:

- *Number of nodes in each cluster*: indicating a **global** representation of attention for a particular region. The more a radiologist spends time on a region, the denser the corresponding cluster is.
- *The amount of time spent on one cluster*: indicating a **local** representation of attention for a cluster. The number of self-loops on each centroid can be considered to define such parameters.

We then defined edge weights based on these two parameters as below:

$$w_{i,j} = \exp(-N_i^2 \times C_{in})^{-1} \times \exp(-N_j^2 \times C_{jn})^{-1}, \quad (5)$$

where N_i and N_j are number of nodes in clusters i and j , respectively, and C_{in} and C_{jn} are number of self-loops for clusters i and j . Each *exp* term can be considered as the attention level corresponding to each of the nodes. The major strength of our modified spectral sparsification algorithm is that we modeled both local and global visual patterns and their interactions through this weight function. The pseudo code of our sparsification method is shown in Algorithm 1.

Algorithm 1: Attention based Spectral Graph Sparsification

Input : Dense graph: $G = (V, E)$, α : Sparsification parameter

Output: Sparse graph: $S = (V, \hat{E}, \hat{w})$

for i and j in V **do**

if *There exists $e_{i,j}$ in E* **then**

 Compute N_i and N_j (number of nodes in clusters corresponding to vertexes i and j)

 Compute C_{in} and C_{jn} (number of self-loops corresponding to vertexes i and j)

 Compute $w_{i,j}$ using eq.5

end

end

return $G(V, E, w)$;

for $e_{i,j}$ in E **do**

 Sample edge $e_{i,j}$ from G with prob. proportional to $w_{i,j} \cdot r_{i,j}$

 Add $e_{i,j}$ to S

end

return $S(V, \hat{E}, \hat{w})$;

To illustrate the effect of our sparsification method on very dense data, we applied the proposed method on synthetic data with different sparsification levels. Results are shown in Fig. 6. The data is created as randomly generated locations which are connected to each other consecutively to best mimic human gaze (in terms of consecutive connections). Progressively sparsified graphs are shown with respect to different levels of edge ratio. *Edge ratio* herein refers to the percentage of the total number of edges remaining after

the sparsification; hence, the most sparse graph is represented on the last column where the edge-ratio is set to 0.2.

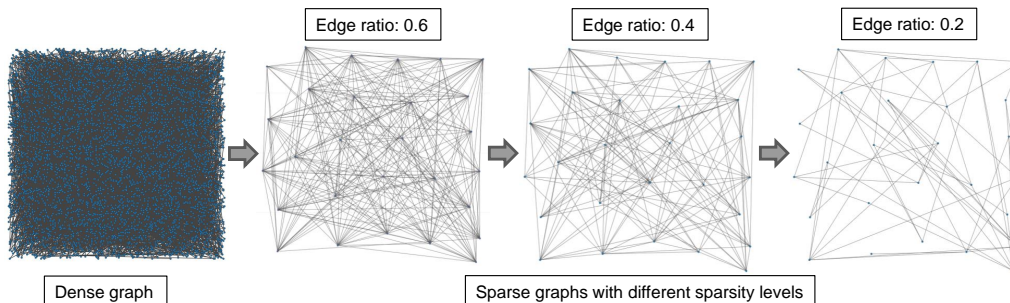


Figure 6: Results of applying proposed graph sparsification method on a 2D dense synthetic data. Edge ratio is the ratio of edges after applying the method to the original graph.

2.5. Step 4: Extracting attention-based ROIs

Having discussed how to construct the sparsified graph while keeping attention information, we will now move on to discuss how to extract the *Regions of Interest (ROIs)* from the graph. This step allows us to combine this information with image content and perform different analysis inside ROIs.

The attention level of each node inside our graph (a_i) can be defined as a combination of global and local attention information on that node. This can be formulated as follows:

$$a_i = \exp(-N_i^2 \times C_{in})^{-1}, \quad (6)$$

where N_i represents the number of nodes in cluster i (i.e., global attention level) and C_{in} represents the number of self loops on cluster i (i.e., local attention level). That is, higher values of a_i correspond to higher focus of attention on a corresponding cluster centroid.

After deciding ROIs, our method enables us to perform any image analysis tasks on the regions of interest including but not limited to segmentation, detection of particular pathology, and diagnosis. In the next section, we demonstrate how the search pattern and attention information from the radiologists' gaze can be combined with image content to perform radiological image analysis: nodule segmentation and false positive removal.

2.6. Step 5: A 3D multi-task deep learning approach for joint nodule segmentation and false positive removal

So far this paper has focused on extracting ROIs from gaze data. The next step is to form the interaction by combining the previous information with an image analysis module. To this end, we propose to use a fully 3D deep multi-task CNN that can perform two image analysis tasks simultaneously. Multi-Task Learning (MTL) is a branch of machine learning that deals with jointly optimizing multiple loss functions to update a single model. The goal of MTL is to generalize a learned model to be able to perform multiple tasks instead of just focusing on one task (Caruana (1998)). Other than having a generalized model, MTL can benefit each task by learning from other tasks. Some underlying features learned from one task can be helpful in increasing the performance of model on another relevant task.

In this work, we propose to combine two relevant tasks of segmentation and false positive (FP) removal using a single 3D CNN. We chose segmentation and FP removal tasks because morphology/volume and shape are important nodules features to distinguish nodules from non-nodules, and decision makers for when to do follow up scan or necessary intervention in routine clinics. Besides, learning a segmentation task in parallel to FP removal task strengthens the effect of such features. In the results section, we show that both tasks benefit from each other and the network performs better on both. This justifies that knowing an abnormality as nodule or non-nodule helps segmentation and the segmentation helps in decision making about nodule vs non-nodule in return.

For the experiment, we briefly feed a 3D volume of interest (VOI) around the cluster centroid corresponding to radiologist’s ROIs into our 3D deep multi-task CNN to perform FP removal and segmentation jointly. The proposed CNN architecture is an encoder-decoder network containing 14 shared layers of which 6 of them are convolutional layers inside the encoder side, and 6 convolutional layers are inside the decoder side. There are also one down sampling and one up-sampling layers. The shared layers are trained jointly for both tasks while task specific layers are trained only on a single task. The network has 3 task specific layers including 1 sigmoid layer, specific to segmentation, and 2 fully connected layers, specific to false positive (FP) removal task. The fully connected layers have 1024 and 2 neurons, respectively.

The input to the network is a 3D volume of size $40 \times 40 \times 6$ centered at the centroid corresponding to the ROIs. The output for FP removal is

the probability of lesion membership to one of the classes (nodule vs. non-nodule) and the output of the segmentation task is a binary mask of a nodule. Our network architecture is inspired by the work of (Badrinarayanan et al. (2017)) and can be considered as an extension of this work into a $3D$ and *multi-task* architecture. The details of our substantially different architecture are demonstrated in Fig. 7.

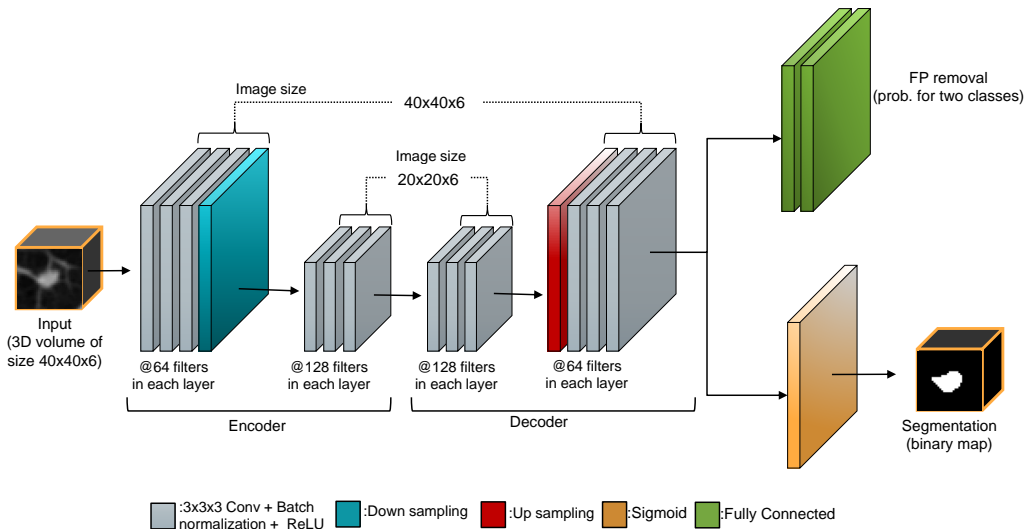


Figure 7: The 3D deep multi-task CNN architecture. The size of all convolutions are $3 \times 3 \times 3$ with a stride of 1 in each dimension. The downsampling and upsampling operators are performed only in the xy plane, and do not affect temporal information. All convolution and layers are $3D$. The network has 14 shared layers, 2 FP removal specific layers and one segmentation specific layer.

3. Results

3.1. Data

We tested our proposed method on synthetic data as well as two datasets obtained from realistic screening experiments:

Synthetic data: Included random generation of 5000 nodes with consecutive generated edges between these nodes, to better mimic the nature of eye-tracking data.

Lung cancer screening: The chest CT scans for this experiment obtained from Lung Tissue Research Consortium (LTRC) (<https://ltrcpublic.com/>).

The in-plane resolution of the images were 512×512 with a voxel size of $0.58 \times 0.58 \times 1.5mm^3$. For training our MTL based CNN, we used the data provided by LUNA challenge (Setio et al. (2017)). The challenge provided the location of nodules accepted by at least 3 out of 4 radiologists. Also, scans with a slice thickness greater than 2.5 mm were excluded from the dataset. Overall, we used 6960 lung nodule ROIs (in 3D) to train/test our network, 3480 of which were positive samples (nodules which were the augmentation of 498 distinct samples) and the rest were negative samples (non-nodule). Positive samples (nodules) were augmented by shifting into 6 directions (top, bottom, left, right, top-left and bottom-right) to keep the balance between classes. The binary masks were obtained manually by a trained annotator using the ITK-SNAP 3D segmentation tool. For MTL-based deep learning experiments, 20% of data was used for testing while the rest was for training, and this procedure was repeated five times to get average score from all experiments.

Participants: Three radiologists with different expertise levels participated in our experiments. Their reading experience levels were noted as 20, 10, and 3 years, respectively. After necessary adjustment and calibrations of eye-tracking equipment done for each participant, they were given instructions about the screening process without letting them know of the existence or absence of tumors in the scans. Mouse and other manipulations (zoom, scroll, contrast/brightness window selection) were recorded automatically by the software along with gaze locations.

3.2. Evaluation of Graph Sparsification

In order to show the effectiveness of our proposed graph sparsification method, we tested it first on a dense synthetic data. Then, a 3D lung screening experiment was conducted for a realistic reading experiment. Also, to show that our algorithm is capable of analyzing multi-screen experiments, we tested the proposed algorithm on a 3D multi-modality MRI prostate cancer screening as a feasibility and proof of concept study. All of our experiments were performed in a realistic radiology room setting without any restriction or limitations on the radiologist. The qualitative and quantitative results of the above-mentioned experiments are reported in the following sections.

3.2.1. Synthetic data experiment:

The goal of this experiment was to show the ability of our proposed method in dealing with very dense data. In the synthetic data, 5000 nodes

were connected consecutively in the $3D$ space to create a dense data. The reason behind consecutive connections is to mimic data recorded from eye-trackers. Figure 8 illustrates the effect of our algorithm in sparsifying the data. The number of edges were reduced from 4269 to 524 in sparsification step, and the number of nodes were reduced from 5000 to 196 in the clustering step.

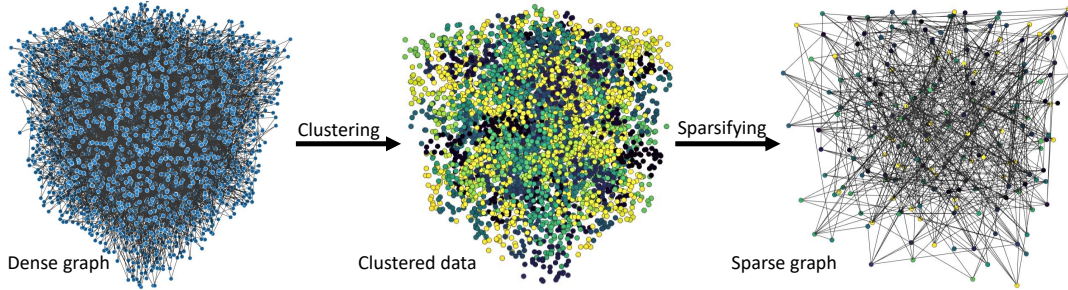


Figure 8: Sparsification results from synthetic data experiments. The number of graph nodes are reduced from 5000 to 196 in the clustering step, and the number of edges (after clustering) are reduced from 4269 to 524 in the graph sparsification step.

3.2.2. Lung cancer screening experiment:

In the lung screening experiments, our participants examined volumetric chest CT scans and the corresponding data was recorded in $3D$ space. The corresponding qualitative results and comparison of search patterns of the three radiologists are reported in Fig. 9. Each column shows one step of the proposed algorithm and each row corresponds to a radiologist. As can be seen, dense graphs which are created using raw data are nearly useless for doing any kind of comparison. However, global comparison of search patterns visually is much easier, as shown in the sparsified graph in the last column. Furthermore, we showed the effect of our sparsification method on the dense eye-tracking data from this experiment in Fig. 10. This figure shows the original gaze points, from 3 radiologists, on the volume renderings of corresponding lung images in the first row. The second row is showing sampled data points after the clustering algorithm. This figure supports how very dense data can be sampled and then be used for any local/global image analysis task easily.

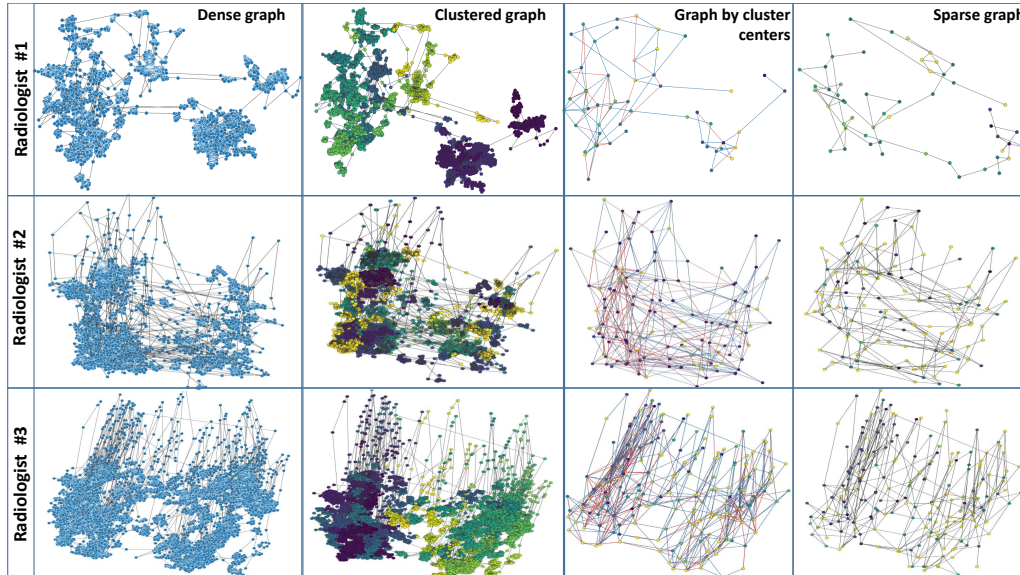


Figure 9: Lung cancer screening experiments with CT data. First column: dense gaze patterns. Second column: attention based clustering. Third column: nodes in clusters are reduced. Fourth column: sparse graph after further reducing edges.

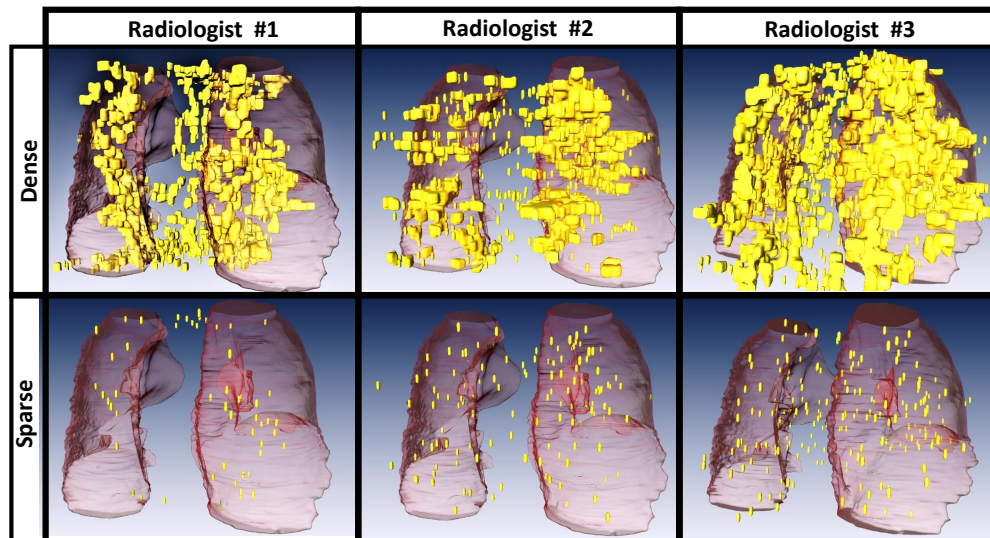


Figure 10: Lung cancer screening experiment with CT data. Dense and sparse gaze points on 3D lung surface.

3.2.3. Sparsification quantitative results:

In order to compare the topology of graphs before and after sparsification, we reported the *Diameter*, *Betweenness*, and *Mean Square Error (MSE)* of the graph Laplacian matrices. All these parameters are well established metrics representing structure of the graphs. *Diameter*: measures the length of maximum shortest path in a graph, *Betweenness*: is a measure of node centrality and counts the number of shortest paths that pass through a node. We reported the Spearman’s rank correlation coefficient to compare betweenness of the original and sparsified graph. *MSE*: compares the structure of the graph before and after sparsification based on the error in the Laplacian matrix of the graph. The results for lung screening data and synthetic data are plotted in Fig. 11 and 12, respectively. The above-mentioned metrics for 3 different radiologists are plotted in Fig. 11. Each point in the plot is computed for an edge ratio. The edge ratio is simply the number of edges in the graph after sparsification over the original graph. As expected by removing more edges (edge ratio drops) betweenness and diameter drop and Laplacian MSE increases.

Also, variation of MSE for the data recorded from 2 radiologists reading 4 different scans were analyzed and plotted in Fig. 13. The MSEs are plotted for the fixed edge ratio of 0.9 in this plot. With a fixed edge ratio higher MSE means that the original graph was more sparse, thus removing the same ratio of edges distorts the graph structure more and results in a higher MSE. Thus, the radiologists’ pattern of search can be compared with this variation. A higher average MSE means the radiologist is doing a less dense search and most probably is more expert due to his/her targeted search pattern.

3.2.4. Evaluation of deep learning based diagnosis algorithm

The proposed Multi-Task network achieved an average Dice Similarity Coefficient (DSC) of 93% for segmentation and 97% accuracy of classification as nodule or non-nodule.

In our experiments, we showed the effect of training segmentation and FP removal tasks jointly versus training them separately. As can be seen in Fig. 14, both tasks benefited from joint training, and each outperformed the best of single task training. The plots indicate the DSC and accuracy over training epochs on test sets (averaged).

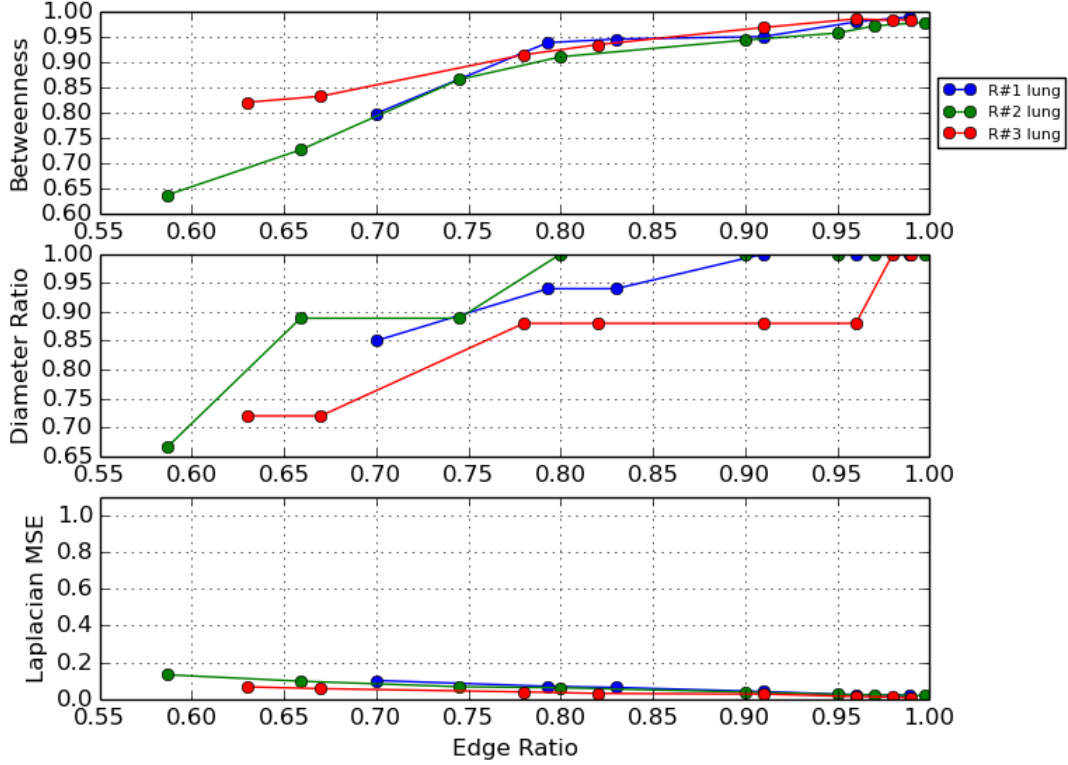


Figure 11: Quantitative parameters to compare graph topology between already clustered data and sparsified data with respect to the preserved edge ratio. (Lung cancer screening experiment)

3.3. Feasibility study of multi-screen eye-tracking:

To show the strength of our proposed sparsification algorithm, we tested it on a multi-screen prostate MR screening experiment. Promising results shows the effectiveness of our algorithm in dealing with more complex tasks including more than one screen.

This experiment was performed on a multi-modality MRI scan of a single subject. The four modalities characteristics are: axial T2 weighted (T2w), with FOV of 140×140 and resolution of $0.27 \times 0.27 \times 3mm^3$, Dynamic Contrast Enhanced (DCE) with FOV of 262×262 and resolution of $1.02 \times 1.02 \times 3$, $b = 2000s/mm^2$, Diffusion Weighted Imaging (DWI) with FOV of 140×140 and resolution of $0.55 \times 0.55 \times 2.73mm^3$. Apparent Diffusion Coefficient

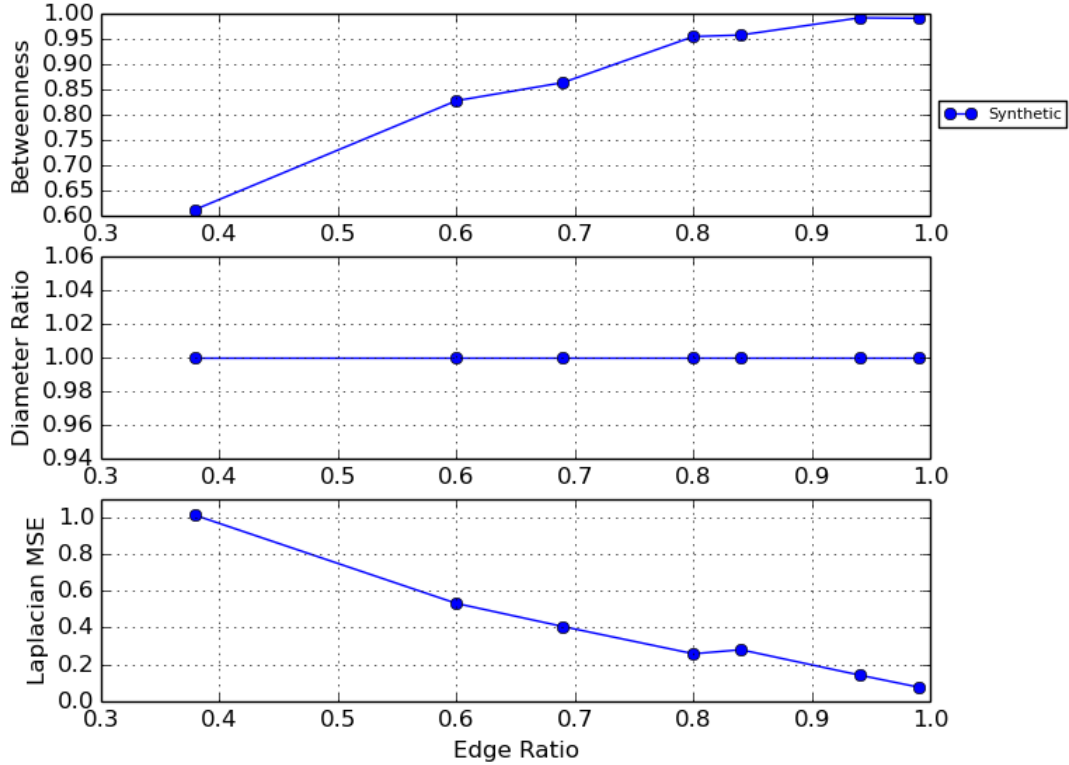


Figure 12: Quantitative parameters to compare graph topology between already clustered data and sparsified data with respect to the preserved edge ratio.(Synthetic data experiment)

(ADC) map was derived from 5 evenly spaced b value ($0 - 750s/mm^2$) DWI.

In this experiment, instead of one single volumetric image, one of our participating radiologists examined a multi-modality 3D prostate MRI scan containing four 3D images. Based on the results reported in Fig. 15, it is clear that the radiologist used axial T2-weighted images (anatomical information) and ADC maps (showing magnitude of diffusion) more frequently than other two images. This observation suggests that although all 4 modalities are being used for making a diagnosis decision T2-weighted and ADC map are more informative to the radiologists in the screening process. This observation can be useful in further developments of automatic computer-aided diagnosis systems.

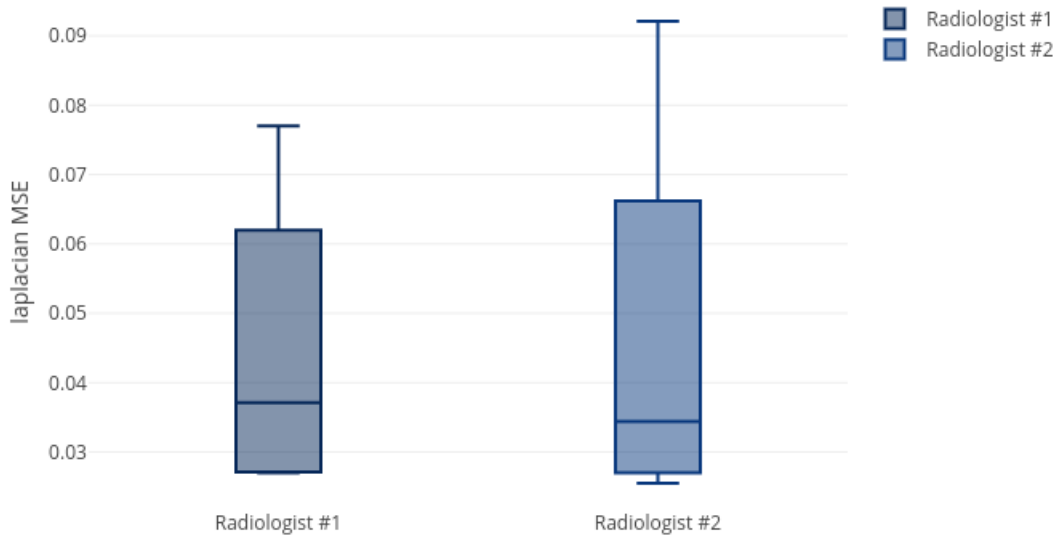


Figure 13: Inter-observer variation of MSE for 2 radiologists on 4 different scans.

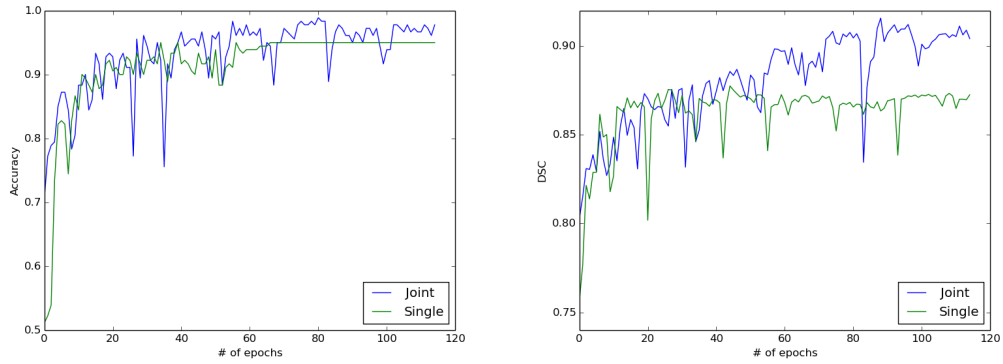


Figure 14: Left: Comparison of accuracy on the test set over training epochs. An increase from 95% to 97% is observed. Right: Comparison of DSC on test set is shown. An increase from 87% to 91% is observed in the network's trained state.

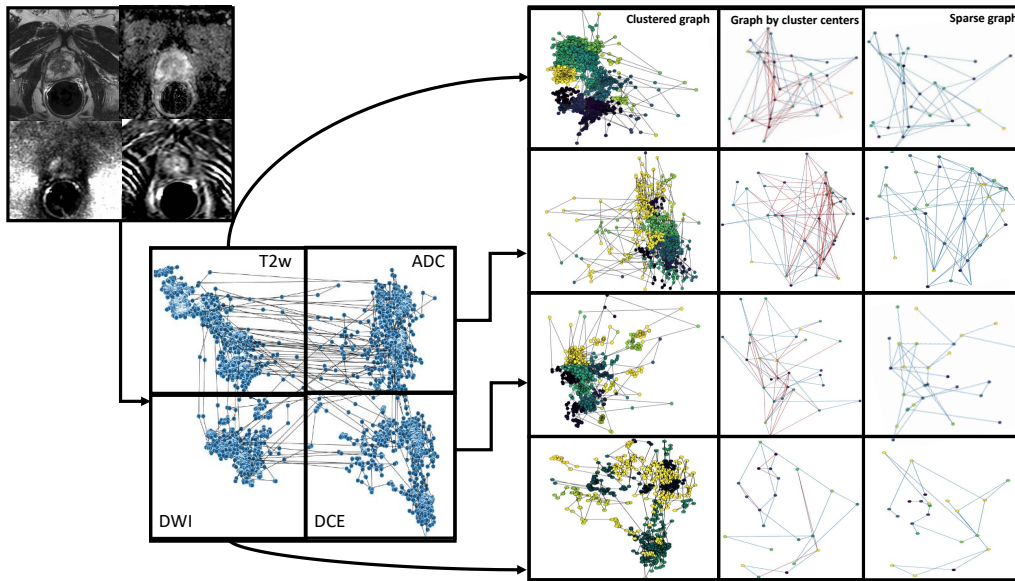


Figure 15: Prostate cancer screening experiments with multi-parametric MRI. Left: four MRI modalities and corresponding dense gaze patterns. Right: Clustered and sparsified gaze patterns corresponding to each modality. First column: clustered dense gaze patterns. Second column: attention based clustering. Third column: sparse graph after further reducing edges.

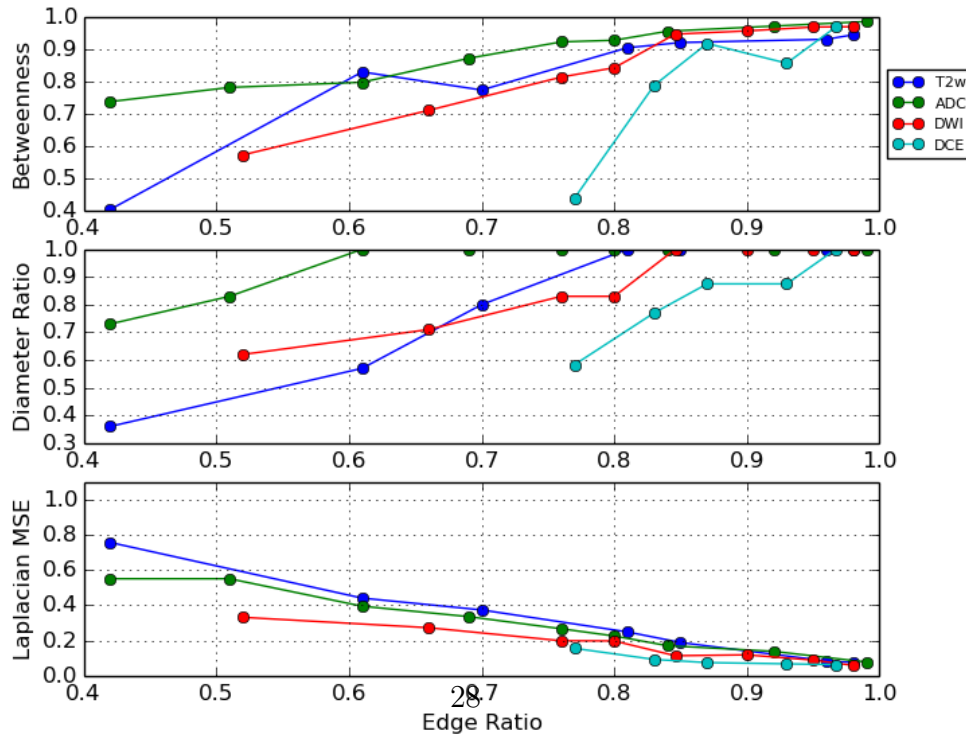


Figure 16: Prostate screening experiment quantitative results.

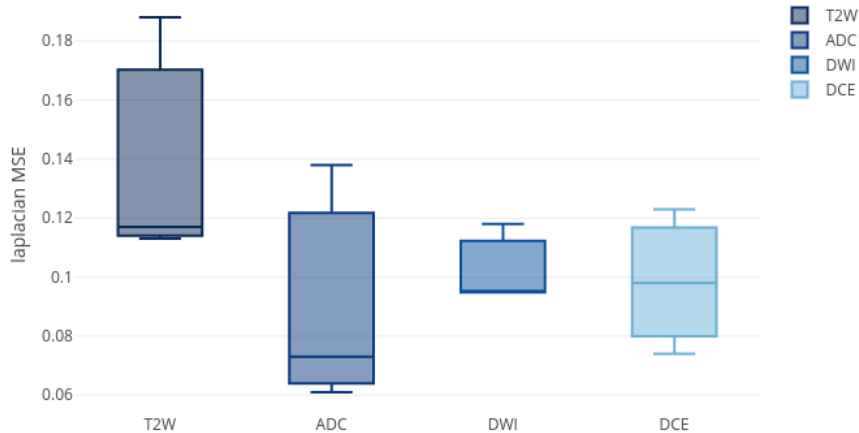


Figure 17: Variation of MSE on different prostate images per modality.

Quantitative results of our method for different modalities as well as the variation over these modalities are shown in Fig. 16 and Fig. 17, respectively. In screening, DWI and DCE modalities were used less than T2 weighted and ADC modalities, therefore, the initial graph representations of the DWI and DCE are less dense compared to those of T2 weighted and ADC. For those less dense graphs, the sparsification algorithm achieved a similar MSE performance in most edge ratios larger than 0.5. From the reason that the sparsification algorithm keeps the graph in a $\sigma - spectral approximation$ of the original graph, we cannot remove large number of edges from less dense graphs. This situation is reflected in diameter ratio and betweenness metrics.

4. Discussions and concluding remarks

As can be interpreted from the lung screening experiment, the less experienced participant has more crowded visual search patterns and examined the most lung volume. Also, from the prostate cancer screening experiment, we observed that radiologists use anatomical/structural information more frequently than other modalities in screening (i.e., diffusion MRI). This can show the importance of anatomical information in prostate cancer detection but at the same time we noticed that where anatomical information gives some cues to radiologists about potential abnormality, radiologists fuse complementary information obtained from other imaging modalities prior to making any diagnostic decisions. Scanpaths across different screens prove this observation (See Fig. 15).

There are some limitations that we would like to mention. One of the limitations of our study is lack of large data for training more sophisticated deep learning models as well as conducting scanpath analysis. The other limitation is in ROI detection. Our system works perfectly with the assumption that the radiologists are examining only lung regions and the ROI falls into the lung. If the radiologist starts focusing on some other areas the segmentation results might not be as desired. To solve this problem we are planning to add another step in our future work that detects lung region and rejects the ROIs outside the lung.

Another limitation of our study is that we did not include parameters (such as radiologist tiredness) that might affect radiologists behavioral patterns. A further study taking into account those parameters and their reliability and impact can lead to much more efficient systems as an extension to what is proposed in this study.

This study offers a new perspective on eye-tracking studies in radiology because of its seamless integration of real radiology experiments and image analysis methods. First, the proposed system models the raw gaze data from eye-tracker as a graph. Then, a novel attention based spectral graph sparsification method is proposed to extract global search pattern of radiologist as well as attention regions. Later, we propose a 3D deep multi-task learning based CNN to perform diagnosis and segmentation tasks jointly inside ROIs. Our proposed sparsification method reduced 90% of data within seconds while keeping mean the square error under 0.1. The segmentation algorithm achieved the average Dice Similarity Coefficient of 91% and classification accuracy for nodule vs. non-nodule was 97%.

CAD systems are often prone to a have high number of false positives findings, which is one of the main drawbacks of such system. Also, missing tumors, especially in their early stages, is very common in screening. To overcome these problems and increase the efficacy of the cancer screening process, we proposed a novel computer algorithm, namely collaborative CAD (C-CAD). Our proposed method takes into account the gaze data of radiologists during the screening process, and incorporates this information into the CAD system for better accuracy in reducing false positive findings in particular. In return, C-CAD has the capability of improving true positive findings as well as reducing missing cases. To the best of our knowledge, there are no previous studies in the literature that systematically and quantitatively include gaze data in the CAD systems. With our proposed attention based graph sparsification method, qualitative comparison and analysis of different

radiologists' visual search patterns (both locally and globally) has become feasible.

Acknowledgement

We would like to thank Nancy Terry, NIH Library Editing Service, for reviewing the manuscript.

References

References

- Al Mohammad, B., Brennan, P., Mello-Thoms, C., 2017. A review of lung cancer screening and the role of computer-aided detection. *Clinical Radiology* 72, 433–442.
- Al-Moteri, M.O., Symmons, M., Plummer, V., Cooper, S., 2017. Eye tracking to investigate cue processing in medical decision-making: A scoping review. *Computers in Human Behavior* 66, 52–66.
- Badrinarayanan, V., Kendall, A., Cipolla, R., 2017. Segnet: A deep convolutional encoder-decoder architecture for scene segmentation. *IEEE transactions on pattern analysis and machine intelligence* .
- Batson, J., Spielman, D.A., Srivastava, N., Teng, S.H., 2013. Spectral sparsification of graphs: theory and algorithms. *Communications of the ACM* 56, 87–94.
- Buty, M., Xu, Z., Gao, M., Bagci, U., Wu, A., Mollura, D.J., 2016. Characterization of lung nodule malignancy using hybrid shape and appearance features, in: *International Conference on Medical Image Computing and Computer-Assisted Intervention*, Springer. pp. 662–670.
- Caroline, C., 2014. Lung cancer screening with low dose ct. *Radiologic clinics of North America* 52, 27.
- Caruana, R., 1998. Multitask learning, in: *Learning to learn*. Springer, pp. 95–133.

- Ciampi, F., de Hoop, B., van Riel, S.J., Chung, K., Scholten, E.T., Oudkerk, M., de Jong, P.A., Prokop, M., van Ginneken, B., 2015. Automatic classification of pulmonary peri-fissural nodules in computed tomography using an ensemble of 2d views and a convolutional neural network out-of-the-box. *Medical image analysis* 26, 195–202.
- Detterbeck, F.C., Mazzone, P.J., Naidich, D.P., Bach, P.B., 2013. Screening for lung cancer: diagnosis and management of lung cancer: American college of chest physicians evidence-based clinical practice guidelines. *CHEST Journal* 143, e78S–e92S.
- Drew, T., Evans, K., V \tilde{o} , M.L.H., Jacobson, F.L., Wolfe, J.M., 2013a. Informatics in radiology: what can you see in a single glance and how might this guide visual search in medical images? *Radiographics* 33, 263–274.
- Drew, T., Vo, M.L.H., Olwal, A., Jacobson, F., Seltzer, S.E., Wolfe, J.M., 2013b. Scanners and drillers: Characterizing expert visual search through volumetric images. *Journal of vision* 13, 3–3.
- Firmino, M., Morais, A.H., Mend \tilde{o} ca, R.M., Dantas, M.R., Hekis, H.R., Valentim, R., 2014. Computer-aided detection system for lung cancer in computed tomography scans: review and future prospects. *Biomedical engineering online* 13, 41.
- van Ginneken, B., Setio, A.A., Jacobs, C., Ciampi, F., 2015. Off-the-shelf convolutional neural network features for pulmonary nodule detection in computed tomography scans, in: *Biomedical Imaging (ISBI), 2015 IEEE 12th International Symposium on, IEEE*. pp. 286–289.
- Grady, L., 2006. Random walks for image segmentation. *IEEE transactions on pattern analysis and machine intelligence* 28, 1768–1783.
- Guo, Y., Gao, Y., Shen, D., 2016. Deformable mr prostate segmentation via deep feature learning and sparse patch matching. *IEEE transactions on medical imaging* 35, 1077–1089.
- Hua, K.L., Hsu, C.H., Hidayati, S.C., Cheng, W.H., Chen, Y.J., 2015. Computer-aided classification of lung nodules on computed tomography images via deep learning technique. *OncoTargets and therapy* 8.

- Hussein, S., Cao, K., Song, Q., Bagci, U., 2017a. Risk stratification of lung nodules using 3d cnn-based multi-task learning, in: International Conference on Information Processing in Medical Imaging, Springer. pp. 249–260.
- Hussein, S., Gillies, R., Cao, K., Song, Q., Bagci, U., 2017b. Tumornet: Lung nodule characterization using multi-view convolutional neural network with gaussian process. arXiv preprint arXiv:1703.00645 .
- Jalalian, A., Mashohor, S.B., Mahmud, H.R., Saripan, M.I.B., Ramli, A.R.B., Karasfi, B., 2013. Computer-aided detection/diagnosis of breast cancer in mammography and ultrasound: a review. *Clinical imaging* 37, 420–426.
- Khosravan, N., Celik, H., Turkbey, B., Cheng, R., McCreedy, E., McAuliffe, M., Bednarova, S., Jones, E., Chen, X., Choyke, P.L., et al., 2016. Gaze2segment: A pilot study for integrating eye-tracking technology into medical image segmentation. *Lecture Notes in Computer Science* .
- Kok, E.M., Jarodzka, H., 2017. Before your very eyes: The value and limitations of eye tracking in medical education. *Medical education* 51, 114–122.
- Kumar, D., Wong, A., Clausi, D.A., 2015. Lung nodule classification using deep features in ct images, in: Computer and Robot Vision (CRV), 2015 12th Conference on, IEEE. pp. 133–138.
- Kundel, H.L., Nodine, C.F., Carmody, D., 1978. Visual scanning, pattern recognition and decision-making in pulmonary nodule detection. *Investigative radiology* 13, 175–181.
- Le, M., Chen, J., Wang, L., Wang, Z., Liu, W., Cheng, K., Yang, X., 2017. Automated diagnosis of prostate cancer in multi-parametric mri based on multimodal convolutional neural networks. *Physics in medicine and biology* .
- Lee, C.S., Nagy, P.G., Weaver, S.J., Newman-Toker, D.E., 2013. Cognitive and system factors contributing to diagnostic errors in radiology. *American Journal of Roentgenology* 201, 611–617.
- Lemaître, G., Martí, R., Freixenet, J., Vilanova, J.C., Walker, P.M., Meriaudeau, F., 2015. Computer-aided detection and diagnosis for prostate

- cancer based on mono and multi-parametric mri: A review. *Computers in biology and medicine* 60, 8–31.
- Littlefair, S., Brennan, P., Reed, W., Mello-Thoms, C., 2017. Does expectation of abnormality affect the search pattern of radiologists when looking for pulmonary nodules? *Journal of digital imaging* 30, 55–62.
- Manning, D., Ethell, S., Donovan, T., Crawford, T., 2006. How do radiologists do it? the influence of experience and training on searching for chest nodules. *Radiography* 12, 134–142.
- McCreadie, G., Oliver, T., 2009. Eight ct lessons that we learned the hard way: an analysis of current patterns of radiological error and discrepancy with particular emphasis on ct. *Clinical radiology* 64, 491–499.
- Roth, H.R., Lu, L., Liu, J., Yao, J., Seff, A., Cherry, K., Kim, L., Summers, R.M., 2016. Improving computer-aided detection using convolutional neural networks and random view aggregation. *IEEE transactions on medical imaging* 35, 1170–1181.
- Samuel G. Armato, I., Li, F., Giger, M.L., MacMahon, H., Sone, S., Doi, K., 2002. Lung cancer: Performance of automated lung nodule detection applied to cancers missed in a ct screening program. *Radiology* 225, 685–692.
- Setio, A.A.A., Ciompi, F., Litjens, G., Gerke, P., Jacobs, C., van Riel, S.J., Wille, M.M.W., Naqibullah, M., Sánchez, C.I., van Ginneken, B., 2016. Pulmonary nodule detection in ct images: false positive reduction using multi-view convolutional networks. *IEEE transactions on medical imaging* 35, 1160–1169.
- Setio, A.A.A., Traverso, A., de Bel, T., Berens, M.S., van den Bogaard, C., Cerello, P., Chen, H., Dou, Q., Fantacci, M.E., Geurts, B., van der Gugten, R., Heng, P.A., Jansen, B., de Kaste, M.M., Kotov, V., Lin, J.Y.H., Manders, J.T., Sónora-Mengana, A., García-Naranjo, J.C., Papavasileiou, E., Prokop, M., Saletta, M., Schaefer-Prokop, C.M., Scholten, E.T., Scholten, L., Snoeren, M.M., Torres, E.L., Vandemeulebroucke, J., Walasek, N., Zuidhof, G.C., van Ginneken, B., Jacobs, C., 2017. Validation, comparison, and combination of algorithms for automatic detection of pulmonary nodules in computed tomography images: The luna16 challenge.

- Medical Image Analysis 42, 1 – 13. URL: <http://www.sciencedirect.com/science/article/pii/S1361841517301020>, doi:<https://doi.org/10.1016/j.media.2017.06.015>.
- Shin, H.C., Roth, H.R., Gao, M., Lu, L., Xu, Z., Nogues, I., Yao, J., Mollura, D., Summers, R.M., 2016. Deep convolutional neural networks for computer-aided detection: Cnn architectures, dataset characteristics and transfer learning. *IEEE transactions on medical imaging* 35, 1285–1298.
- Siegel, R.L., Miller, K.D., Jemal, A., 2017. Cancer statistics, 2017. *CA: A Cancer Journal for Clinicians* 67, 7–30. URL: <http://dx.doi.org/10.3322/caac.21387>, doi:10.3322/caac.21387.
- Spielman, D.A., Srivastava, N., 2011. Graph sparsification by effective resistances. *SIAM Journal on Computing* 40, 1913–1926.
- Tourassi, G., Voisin, S., Paquit, V., Krupinski, E., 2013. Investigating the link between radiologists’ gaze, diagnostic decision, and image content. *Journal of the American Medical Informatics Association* 20, 1067–1075.
- Tsehay, Y., Lay, N., Wang, X., Kwak, J.T., Turkbey, B., Choyke, P., Pinto, P., Wood, B., Summers, R.M., 2017a. Biopsy-guided learning with deep convolutional neural networks for prostate cancer detection on multiparametric mri, in: *Biomedical Imaging (ISBI 2017), 2017 IEEE 14th International Symposium on, IEEE*. pp. 642–645.
- Tsehay, Y.K., Lay, N.S., Roth, H.R., Wang, X., Kwaka, J.T., Turkbey, B.I., Pintob, P.A., Woodc, B.J., Summersa, R.M., 2017b. Convolutional neural network based deep-learning architecture for prostate cancer detection on multiparametric magnetic resonance images, in: *SPIE Medical Imaging, International Society for Optics and Photonics*. pp. 1013405–1013405.
- Venjakob, A.C., 2015. Visual search, perception and cognition when reading stack mode cranial ct .
- Venjakob, A.C., Marnitz, T., Phillips, P., Mello-Thoms, C.R., 2016. Image size influences visual search and perception of hemorrhages when reading cranial ct an eye-tracking study. *Human Factors: The Journal of the Human Factors and Ergonomics Society* , 0018720816630450.

- Venjakob, A.C., Mello-Thoms, C.R., 2016. Review of prospects and challenges of eye tracking in volumetric imaging. *Journal of Medical Imaging* 3, 011002–011002.
- Zhang, T., Ramakrishnan, R., Livny, M., 1996. Birch: an efficient data clustering method for very large databases, in: *ACM Sigmod Record*, ACM. pp. 103–114.